

## Supplemental Material

# Magma recharging beneath the Weishan volcano of the intraplate Wudalianchi volcanic field, northeast China, implied from 3D magnetotelluric imaging

Ji Gao<sup>1</sup>, Haijiang Zhang<sup>1,6\*</sup>, Senqi Zhang<sup>2</sup>, Hailiang Xin<sup>1,5</sup>, Zhiwei Li<sup>3</sup>, Wei Tian<sup>4</sup>, Feng Bao<sup>3</sup>, Zhengpu Cheng<sup>2</sup>, Xiaofeng Jia<sup>2</sup>, and Lei Fu<sup>2</sup>

<sup>1</sup>*Laboratory of Seismology and Physics of Earth's Interior, School of Earth and Space Sciences, University of Science and Technology of China, Hefei, China*

<sup>2</sup>*Center for Hydrogeology and Environmental Geology, CGS, Baoding, China*

<sup>3</sup>*State Key Laboratory of Geodesy and Earth's Dynamics, Institute of Geodesy and Geophysics, CAS, Wuhan, China*

<sup>4</sup>*The Key Laboratory of Orogenic Belts and Crustal Evolution, Ministry of Education, School of Earth and Space Sciences, Peking University, Beijing, China*

<sup>5</sup>*Geophysical Exploration Center, CEA, Zhengzhou, China*

<sup>6</sup>*Mengcheng National Geophysical Observatory, University of Science and Technology of China, Hefei, Anhui, China*

*\*correspondence to: zhang11@ustc.edu.cn*

### **This PDF file includes:**

Supplemental Text Sections 1 to 5

Supplemental Figs.S1 to S13

# Supplemental Text

## 1. 3D MT Inversion Details and Interpretation of Low Resistivity by Magmas

We adopt the package ModEM developed by Egbert and Kelbert (2012) and Kelbert et al. (2014) for the 3D MT inversion. Because topography variations ( $< \sim 200$  m) are much smaller than the study region ( $\sim 20$  km by 30 km), the inversion does not consider the topography effect. For the 3D MT inversion, the resistivity model is discretized with  $48 \times 63$  horizontal blocks and 51 vertical blocks. In the horizontal plane, the grid interval is 500 m in the central region to ensure that there is a free grid node between the two MT sites. In the vertical direction, the cell thickness is 20 m near the surface and is increased with a rate of 1.2 as depth increasing to 576 km.

The inversion uses the off-diagonal resistivity and phase components for 20 periods in the frequency range of 320 to  $3.4 \times 10^{-4}$  Hz. Before the inversion, we first removed the noisy data by a visual program, and then a 5% error floor for resistivity and a 1.43 arc degree error floor for phase components were imposed. The initial resistivity was set to be  $100 \Omega \cdot \text{m}$  in a homogeneous half space. The normalized root mean square (RMS) value of data misfit decreased from 6.0989 to 1.3990 after 112 iterations. The data fitting between synthetic and observed response curves is very good for resistivity and phase tensors at 10 selected locations (Figure 2a, Figure S1). Additional inversions using different combinations of MT data, different starting models, and different error floors are also tested (Figures S2-S4), which indicate that the above selected inversion parameters are relatively optimal.

Both Figure 2 and Figure 3 show clearly low resistivity anomalies beneath the WS volcano. It can be seen that the low resistivity anomalies in the depth zone of 2-6 km tend to be distributed in the NW-SE strike, as supported by the phase tensor analysis at the period of 1.4 s. In comparison, the low resistivity anomalies in the deeper part are much larger and are comparable to the aperture of the MT sites. The phase tensor analysis at the period of 11.2s also supports (Figure S9) these observations, which corresponds to the depth of 5-17 km for the 10-100 ohm-m earth. It can be seen that  $\_ \Phi_{min}$  values are generally greater than 45 degrees at most of sites, indicating there exist low resistivity anomalies beneath the MT sites. Compared to induction vectors at 1.4 s, they also point away from the volcano at most sites but with more heterogeneous directions. Because both aqueous fluids and magmas can cause low resistivity and low velocity anomalies, it is possible that low resistivity anomaly body could be associated with aqueous fluids. However, as seen in Figure 3, the earthquakes are all located outside low resistivity anomalies. This can be interpreted that these low resistivity anomalies are associated with high temperature greater than the brittle-ductile transition. In many other volcanoes, the

imaged low resistivity anomalies beneath ~3-4 km are also generally interpreted to be magma reservoirs (e.g., Hill et al., 2015). For these reasons, similar to Li et al. (2016), we interpret low resistivity anomalies below ~2-4 km as magma reservoirs. The volume enclosed by the iso-surface of low resistivity value of  $3 \Omega \cdot \text{m}$  is approximately  $102 \text{ km}^3$ . For magma bodies above the solidus in the upper crust, the magma intrusion rate is required to be greater than  $10^{-4} \text{ km}^3/\text{yr}$  (Karakas et al., 2017). For the case of the WS volcano, assuming the magma accumulation started after the last eruption ~50 Ka ago, the magma intrusion rate is estimated to be  $\sim 2 \times 10^{-3} \text{ km}^3/\text{yr}$  to accumulate the magma volume of  $102 \text{ km}^3$ . The magma intrusion rate could be greater than this value because the volume is likely underestimated, as suggested by the synthetic test. Therefore, beneath the WS volcano the magma bodies can be above the solidus.

## 2. Estimating Melt Fractions Based on the Resistivity Anomalies

The VFT (Vogel-Fulcher-Tammann) equation (Fulcher, 1925) modified by Ni et al. (2011) can be used to obtain the temperature dependent basalt conductivity for basaltic melt, as follows,

$$\log \sigma = 2.172 - \frac{860.82 - 204.46\sqrt{w}}{T - 1146.8}, \quad (1)$$

where  $\sigma$  is the electrical conductivity of basalt melt in S/m,  $T$  is the temperature in K, and  $w$  is the water ( $H_2O$ ) content in wt%. The temperature of magmas shortly before eruption for the WVF was estimated to be in the range of  $1050\text{-}1200^\circ$  (Lv, 1994) or  $1250^\circ$  (Kuritani et al., 2013), thus we use the temperature at  $1200^\circ$  ( $1473\text{K}$ ) for estimation.

For two phases of melt and solid rock, the bulk conductivity can be calculated using HS+ model of Glover and Hole et al. (2000), as follows,

$$\sigma = \sigma_2 \left[ 1 - \frac{3F_1(\sigma_2 - \sigma_1)}{3\sigma_2 - F_2(\sigma_2 - \sigma_1)} \right], \quad (2)$$

where  $\sigma$  is the bulk conductivity which can be calculated from the two individual conductivities of solid rock ( $\sigma_1$ ), and melt ( $\sigma_2$ ), and the volume fractions ( $F_1$ ,  $F_2$ ) of the two phases. With the fixed temperature of  $1473\text{k}$  and conductivity of solid rock  $\sigma_1$  ( $0.001 \text{ S/m}$ ), we calculated the bulk conductivities by varying melt fractions and water contents, respectively (Figure 4c). In Figure 4c, the contour line for bulk conductivity of  $0.3 \text{ S/m}$  indicates the trade-off between melt fractions and water contents. To get the bulk

conductivity of 0.3 S/m, the corresponding melt fraction would be 40.9%, 28.1%, 16.2%, 7.2% and 3.8% for basaltic melt with water contents of 0.5wt%, 1.0 wt%, 2.0 wt%, 4.0 wt% and 6.0 wt%, respectively.

Because of the coupling between melt fraction and water content, in order to estimate the melt fraction, we should first get the knowledge of the water content. For the WVF, Xia (1990) estimated the magma contains 2-4wt% water and Kuritani et al. (2013) estimated the water content to be greater than 1.1-2.2wt%. Recently, Di et al. (2019) applied a new basalt hygrometer to the WVF and constrained the pre-eruption H<sub>2</sub>O content of the magma to be  $4.5 \pm 1.2$  wt% at a pressure range of 10.1-13.5 kbar. Based on H<sub>2</sub>O-CO<sub>2</sub> solubility model of Duan (2014), the H<sub>2</sub>O content of the magma equilibrated at 0.8 kbar (~2.5km depth, Figure S10) would be 2.1wt% after an open system degassing or 2.4 wt% after a closed system degassing. Therefore, water content for magma beneath the WS volcano is estimated to be 2.1-2.4 wt%. To reach the resistivity of  $0.3\Omega \cdot m$  melt fraction in the magma reservoirs is estimated to be 15.4-13.4 wt% (Figure 4c).

### 3. Estimating Melt Fractions Based on the Seismic Velocity Anomalies

Here we follow the method used in Chu et al. (2010) to estimate melt fraction using the V<sub>s</sub> model derived from ambient noise tomography of Li et al. (2016).

The effective elastic moduli of fluid-saturated porous materials can be calculated using Gassmann's relations (Gassmann, 1951), as follows:

$$\mu_{eff} = \mu_{dry}, \quad (3)$$

where  $\mu_{eff}$  is the effective shear modulus for the material of the frame rock, and  $\mu_{dry}$  is the shear modulus of the drained matrix. Critical melt fraction defines the transition from a medium that is supported by the frame to a medium where solid materials are suspended in the fluid. For porosity below the critical value,

$$\mu_{dry} = \mu_0 \left(1 - \frac{\phi}{\phi_c}\right), \quad (4)$$

where  $\phi_c$  is the critical porosity,  $\phi$  is the porosity, and  $\mu_0$  is the shear modulus for the granite. For granite, laboratory measurement suggests that the  $\phi_c$  is 0.35 (van der Molen and Paterson, 1979). Density and seismic velocity of the fluid-filled porous material can be calculated as follows,

$$\rho_{eff} = (1 - \phi) + \phi \sum S_i \rho_i \quad (5)$$

$$V_s = \sqrt{\frac{\mu_{eff}}{\rho_{eff}}}, \quad (6)$$

where  $\rho_{eff}$  is the effective density for the material of the frame rock, and  $S_i$ ,  $\rho_i$  are individual fluid saturation and density, respectively.

With shear wave velocity  $V_s$  and density  $\rho$ ,  $\mu_0$  can be represented as follows,

$$\mu_0 = V_s^2 \cdot \rho \quad (7)$$

By using equations (3)-(7) and parameters in Table DR1, we can estimate the shear wave velocities with different melt saturations (Figure 4d).

**Table S1.** Physical properties of granite and basalt melt (modified from Chu et al., (2010))

Material	Vp(km/s)	Vs(km/s)	$\rho$ (g/cm <sup>3</sup> )
granite	5.70	3.40	2.63
basalt melt	2.65	0.0	2.20

#### 4. Earthquake activity around the WS volcano

We first assembled the earthquake locations around the WS volcano from the China Earthquake Administration (CEA) catalogue for the period of 1980-2019 (Figure DR12a). It is noted that except for the year of 1986, overall the earthquake activity is increased after 1996. This is mainly because a new seismic station was added in the region in 1996. To better locate earthquakes around the WS volcano, we requested seismic waveforms on regional permanent seismic stations for 101 earthquakes that were available from the CEA Data Center from 2008 to 2019 (Figure S12b). We manually picked P and S first arrivals on earthquake waveforms and located them by using the regional version of tomoDD code (Zhang and Thurber, 2003). The  $V_p$  and  $V_s$  models used for location are extracted from the USTClitho1.0 model of Xin et al. (2019). For the initial earthquake locations from the CEA catalogue, the RMS travel time residual is 1.44 s. after location, the RMS travel time residual is decreased to 0.14 s, indicating the earthquake locations are much improved.

In addition, we also assembled continuous data recorded by 15 temporary seismic stations from dense array around the WS volcano of Li et al. (2016). We detected 7 seismic events around the WS volcano (Figure S13a), among which some clearly show the characteristic volcanic tremor signals (Figure S13d-h). This further indicates that seismic activity in the WVF is much more active than the CEA catalogue suggested.

#### 5. Interpretation of WS volcano without apparent hydrothermal alterations

It seems paradoxical there exist shallow magma reservoirs beneath the WS volcano without apparent hydrothermal alterations (Lv, 1994). For example, the Keyan spring located on the western edge of the WS cone has the temperature of 3°. On average, Keyan cold spring erupts 279.3 m<sup>3</sup> CO<sub>2</sub> on a daily basis. Based on the isotopic analysis, the continuous emission of CO<sub>2</sub> has the origin at upper mantle (Lv, 1994), indicating the WS volcano is active. When this deeply generated CO<sub>2</sub> is diffused to near surface, it can absorb heat with the phase change from the super-critical state (Zhang et al., 2017), which could partly contribute to the formation of the cold spring. In addition, this can be further explained by a barrier layer above ~2 km separating shallow magma reservoirs from the surface. From seismic and MT imaging results (Figure 3), this barrier layer is associated with relatively higher resistivity and lower velocity. The local geological survey found ignimbrite as one component of the shallow formation (Zhang et al., 2017). It is likely that ignimbrite alternated by sediments, combined with relatively higher concentration of CO<sub>2</sub> in the shallower part, could act as a good heat insulator preventing heat from magma reservoirs conducted to the surface, which would have the physical property of low  $V_s$  and high resistivity.

## References

- 1) Chu, R., Helmberger, D.V., Sun, D., Jackson, J.M., and Zhu, L., 2010, Mushy magma beneath Yellowstone: Geophysical Research Letters, v. 37, L01306, [doi:10.1029/2009GL041656](https://doi.org/10.1029/2009GL041656).
- 2) Di Y. K., Tian W., Chen M., Li Z. F., Chu Z. Y., and Liang J., 2019. A method to estimate the pre-eruptive water content of basalts: application to the Wudalianchi–Erkeshan–Keluo volcanic field, Northeastern China. *American Mineralogist*, [doi:10.2138/am-2020-7137](https://doi.org/10.2138/am-2020-7137).
- 3) Duan, X., 2014 A general model for predicting the solubility behavior of H<sub>2</sub>O-CO<sub>2</sub> fluids in silicate melts over a wide range of pressure, temperature and compositions. *Geochimica et Cosmochimica Acta*, 125, 582-609, [doi.org/10.1016/j.gca.2013.10.018](https://doi.org/10.1016/j.gca.2013.10.018).
- 4) Egbert, G. D., and Kelbert, A., 2012, Computational recipes for electromagnetic inverse problems. *Geophysical Journal International*, 189(1), 251-267, [doi:10.1111/j.1365-246X.2011.05347.x](https://doi.org/10.1111/j.1365-246X.2011.05347.x).
- 5) Fulcher, G. S., 1925, Analysis of recent measurements of the viscosity of glasses. *Journal of the American Ceramic Society*, 8(6), 339-355, [doi:10.1111/j.1151-2916.1925.tb16731.x](https://doi.org/10.1111/j.1151-2916.1925.tb16731.x).
- 6) Gassmann, F., 1951. Über die elastizität poroser medien. *Vierteljahrsschrift der Naturforschenden Gesellschaft in Zurich*, 96, 1-23.
- 7) Glover, P. W., Hole, M. J., and Pous, J., 2000, A modified Archie's law for two conducting phases. *Earth and Planetary Science Letters*, 180(3-4), 369-383, [doi:10.1016/S0012-821X\(00\)00168-0](https://doi.org/10.1016/S0012-821X(00)00168-0).
- 8) Karakas, O., Degruyter, W., Bachmann, O., Dufek, J., 2017. Lifetime and size of shallow magma bodies controlled by crustal-scale magmatism. *Nature Geoscience*, 10(6), 446, [doi:10.1038/NNGEO2959](https://doi.org/10.1038/NNGEO2959).
- 9) Kelbert, A., Meqbel, N., Egbert, G. D., and Tandon, K., 2014, ModEM: A modular system for inversion of electromagnetic geophysical data. *Computers & Geosciences*, 66, 40-53, [doi:10.1016/j.cageo.2014.01.010](https://doi.org/10.1016/j.cageo.2014.01.010).
- 10) Kuritani, T., Kimura, J. I., Ohtani, E., Miyamoto, H., and Furuyama, K., 2013, Transition zone origin of potassic basalts from Wudalianchi volcano, northeast China. *Lithos*, 156, 1-12, [doi:10.1016/j.lithos.2012.10.010](https://doi.org/10.1016/j.lithos.2012.10.010).
- 11) Li, Z., Ni, S., Zhang, B., Bao, F., Zhang, S., Deng, Y., and Yuen, D. A., 2016, Shallow magma chamber under the Wudalianchi Volcanic Field unveiled by seismic imaging with dense array. *Geophysical Research Letters*, 43(10), 4954-4961, [doi:10.1002/2016GL068895](https://doi.org/10.1002/2016GL068895).
- 12) Lv Z. W., 1994, Volcanic structure of the present day volcanic group Wudalianchi and its forming mechanism. *Volcanology & Mineral Resources*, 15(1):6-21.

- 13) Ni, H., Keppeler, H., and Behrens, H., 2011, Electrical conductivity of hydrous basaltic melts: implications for partial melting in the upper mantle. *Contributions to Mineralogy and Petrology*, 162(3), 637-650, [doi:10.1007/s00410-011-0617-4](https://doi.org/10.1007/s00410-011-0617-4).
- 14) Van der Molen, I., & Paterson, M. S., 1979. Experimental deformation of partially-melted granite. *Contributions to Mineralogy and Petrology*, 70(3), 299-318, [doi:10.1007/BF00375359](https://doi.org/10.1007/BF00375359).
- 15) Xia, L. Q., 1990. On the evolution of volcanic magma from Wudalianchi, China. *Acta Petrologica Sinica*, 1, 13-29.
- 16) Zhang, S. Q., Jia, X. F., Zhang, Y., Li, S. T., Li, Z. W., Tian, P. Y., Ming, Y. Y., Zhang, C., 2017. Volcanic magma chamber survey and geothermal geological condition analysis for hot dry rock in the Weishan volcano in Wudalianchi region, Heilongjiang province. *Acta Geologica Sinica*, 91(7), 1506-1521.

## Supplemental Figures

- Figure S1. Comparison of measured and calculated MT data at selected MT sites.
- Figure S2. Comparison of data fitting at the MT site 2–10 for inversions with different inversion components.
- Figure S3. Comparison of data fitting for apparent resistivity and phase at the MT site 2–10 with different initial homogeneous resistivity models.
- Figure S4. Comparison of the inverted models using different error floors of 3%, 5%, 10% and 15% for resistivity and phase values.
- Figure S5. Sensitivity test for the conductivity body under the WS volcano.
- Figure S6. Synthetic test for a 3D model with low resistivity anomaly extended to 15 km depth.
- Figure S7. Synthetic test for a 3D model with low resistivity anomaly extended to 8km.
- Figure S8. Synthetic test for a 3D model with low resistivity anomaly extended to 45km depth.
- Figure S9. Distribution of MT phases tensors at each site for the period of 11.2s.
- Figure S10. Modelled H<sub>2</sub>O-CO<sub>2</sub> degassing curves for the WVF magma.
- Figure S11. Melt fraction estimation based on the velocity anomalies along the section AA'.
- Figure S12. Earthquake activity around the WS volcano.
- Figure S13. Distribution of selected seismic stations of temporary seismic array around the WS volcano of Li et al. (2016) and detected events, as well as their waveforms.

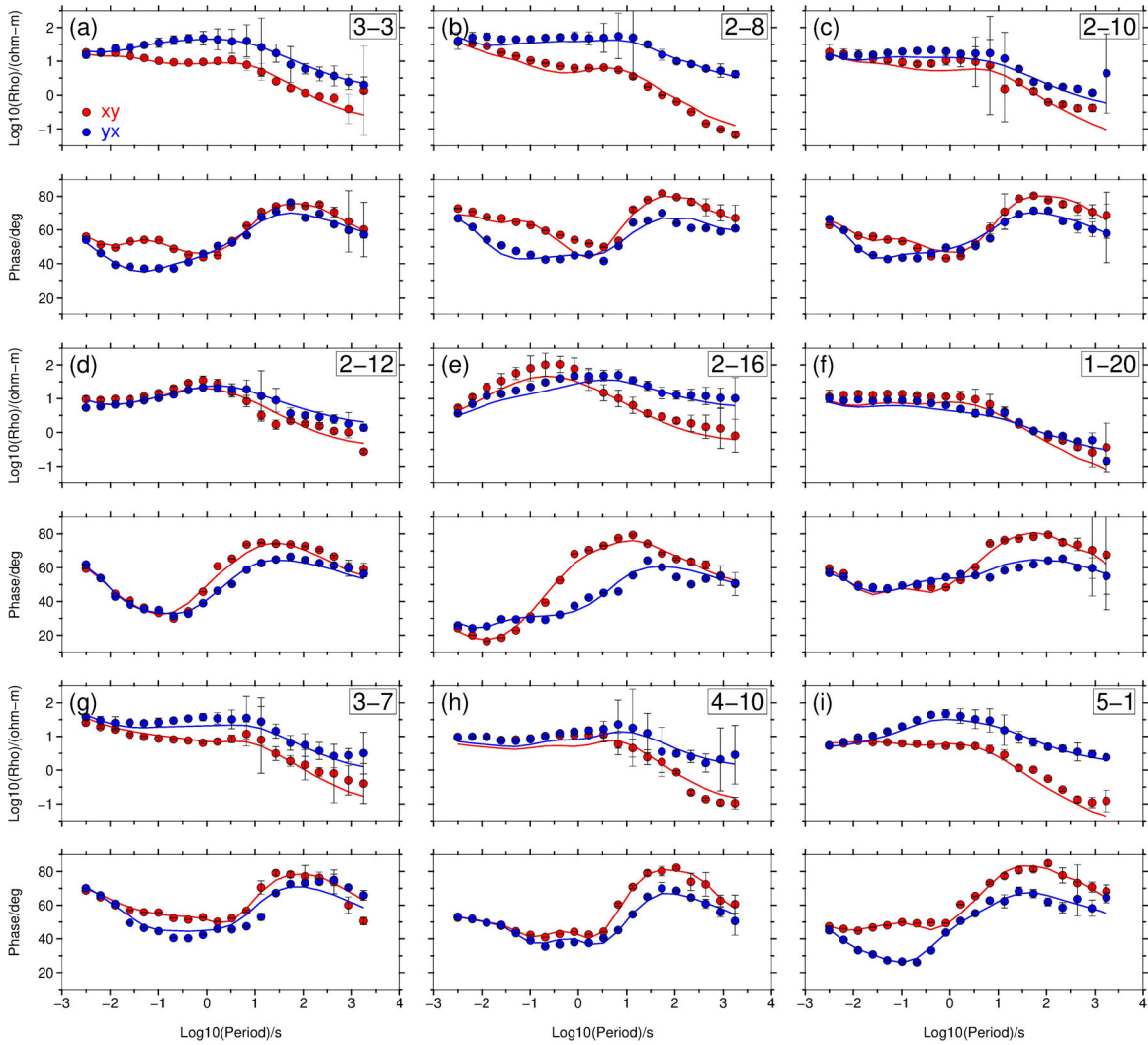


**Figure S1.** Measured and calculated apparent resistivity and phase curves with error bars for ten MT sites. Locations for the ten sites (a-i) are shown in Figure 2a. Red lines and squares represent  $xy$  oriented observations and responses of  $\text{Rho}_{xy}$  and  $\text{Phase}_{xy}$ , respectively. Blue lines and triangles represent  $yx$  oriented observations and responses of  $\text{Rho}_{yx}$  and  $\text{Phase}_{yx}$ , respectively.

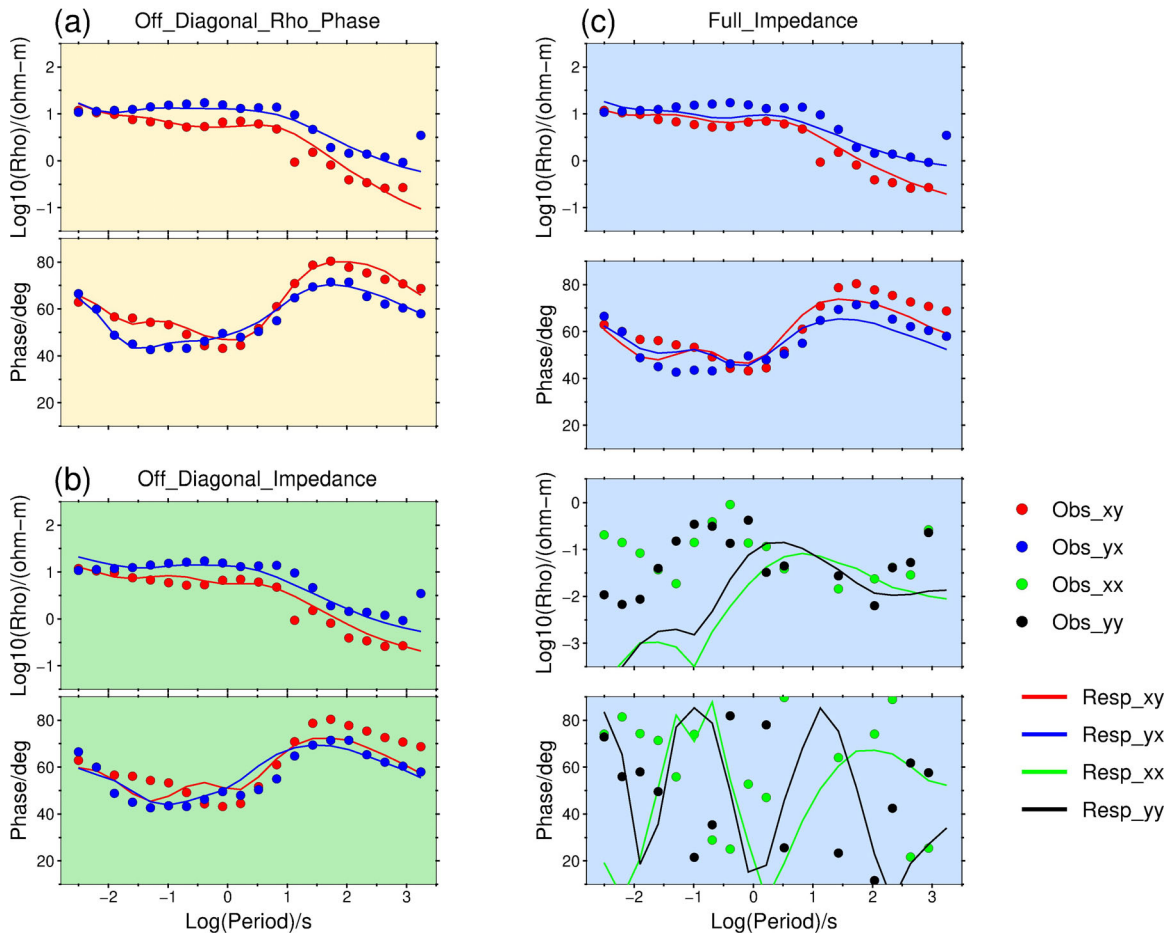


**Figure S2.** Comparison of data fitting at the MT site 2–10 (shown in Figure DR5) for inversions with different inversion components. (a) Inversion using off-diagonal resistivity and phase components (ModEM inversion option Off\_Diagonal\_Rho\_Phase). (b) Inversion using off-diagonal impedance components (ModEM inversion option Off\_Diagonal\_Impedance). (c) Inversion using full impedance components (ModEM inversion option Full\_Impedance). The circles with red, blue, green and black colors represent observed components of XY, YX, XX and YY, respectively. The lines with red, blue, green and black colors represent theoretical responses for XY, YX, XX and YY components, respectively. In comparison, inversion using off-diagonal resistivity components has the best data fitting for the main diagonal components (XY and YX), while inversion using full impedance components cannot fit XX and YY components well. For this reason, inversion using off-diagonal resistivity components is preferred.

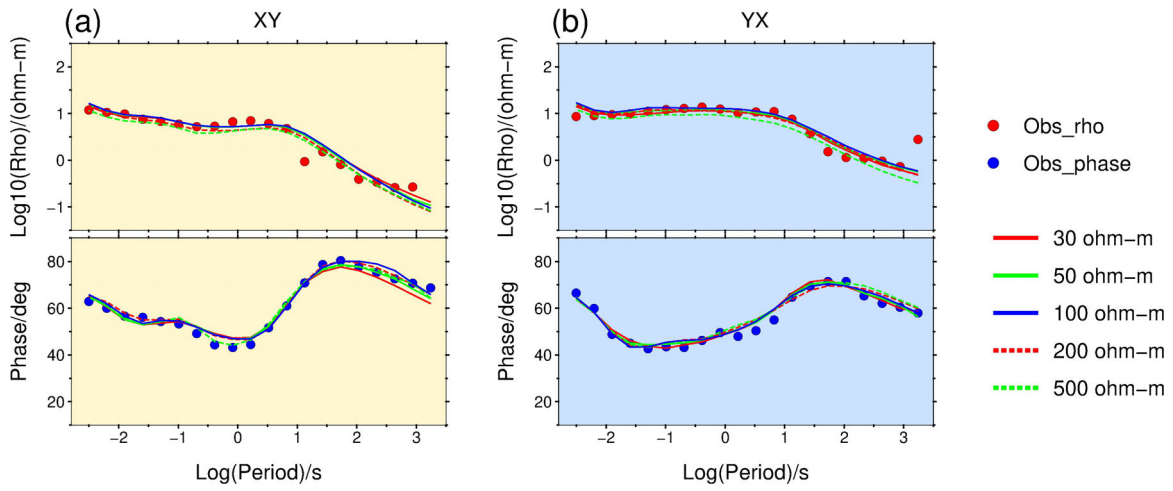


**Figure S3.** Comparison of data fitting for (top) resistivity (bottom) and phase at the MT site 2–10 (shown in Figure DR5) with different initial homogeneous resistivity models of 30 ohm-m, 50 ohm-m, 100 ohm-m, 200 ohm-m and 500 ohm-m. The initial resistivity model with 100 ohm-m has the best data fitting. (a) XY component; (b) YX component.

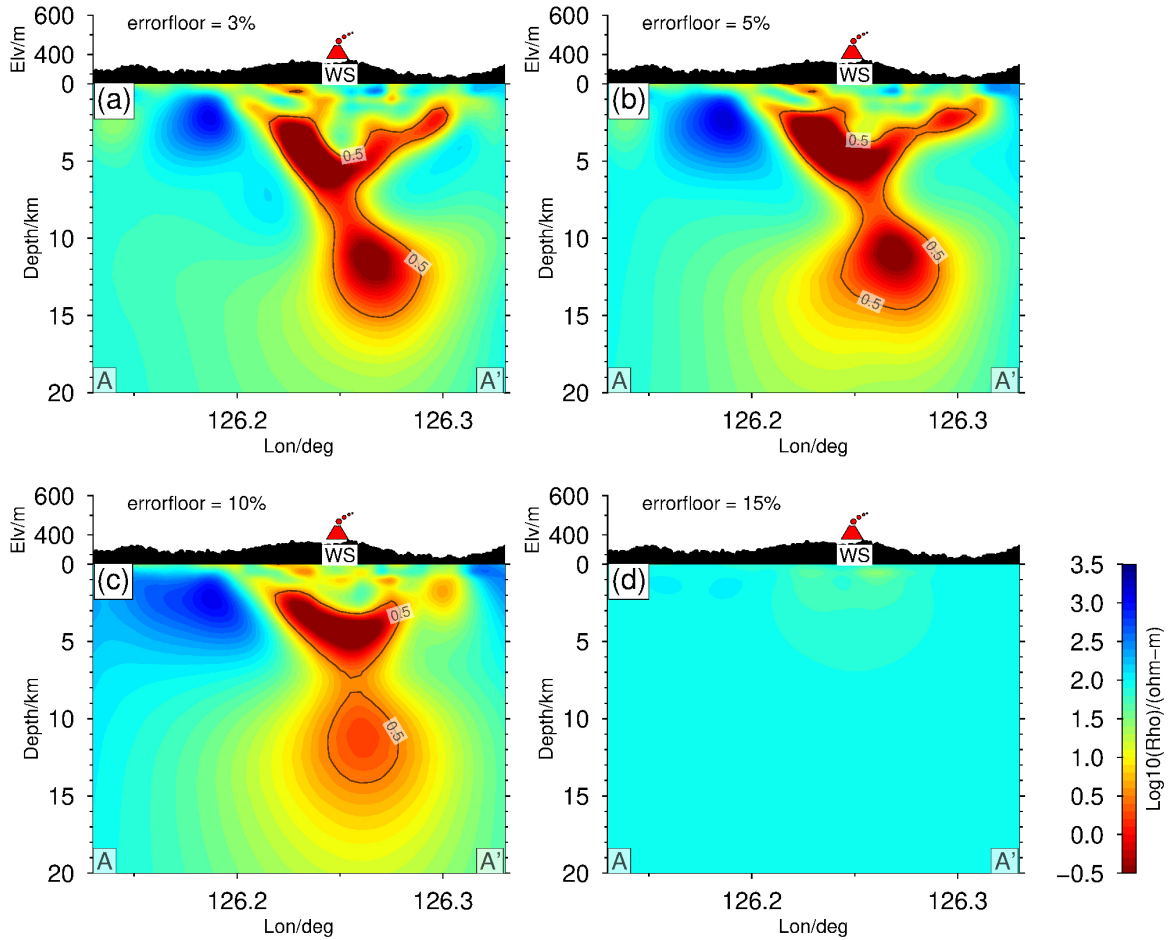


**Figure S4.** Comparison of the inverted models using different error floors for resistivity and phase values. Error floors of 3%, 5%, 10% and 15% are tested, respectively. When the error floor is set to be 3%, the root mean square (RMS) data residual decreases from 9.4637 to 2.1376 with 113 iterations. When the error floor is set to be 5%, the RMS data residual decreases from 6.0989 to 1.3990 with 112 iterations. When the error floor is set to be 10%, the RMS data residual decreases from 3.2598 to 1.0424 with 41 iterations. When the error floor is set to be 15%, the RMS data residual decreases from 2.3181 to 2.087 with 42 iterations. In comparison, inversion with error floor of 5% has an appropriate normalized data residual.

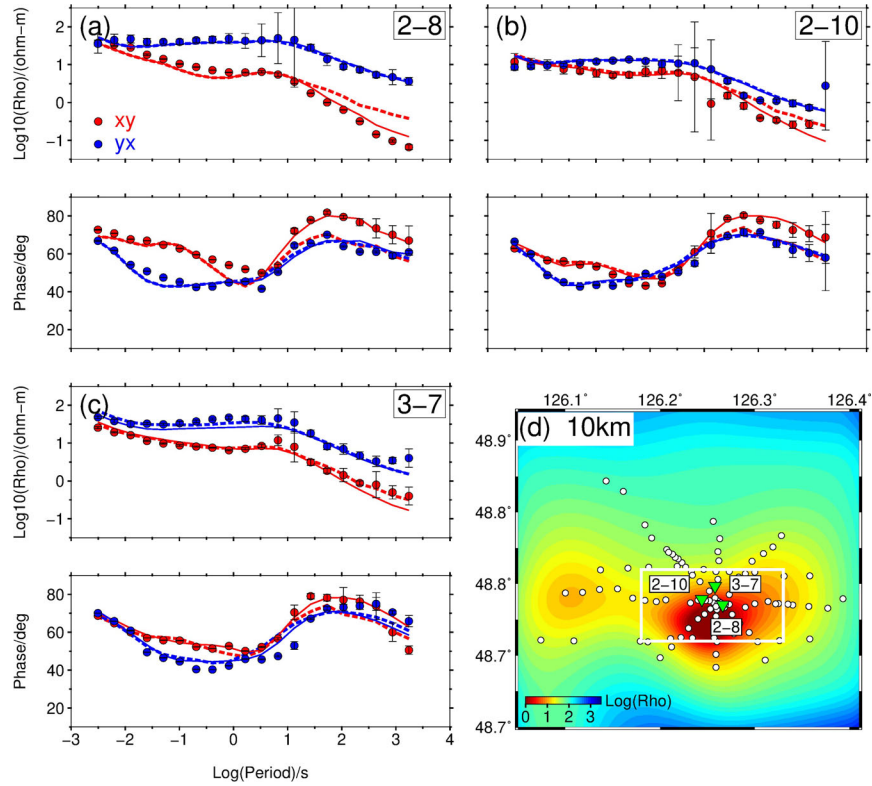


**Figure S5.** Sensitivity test for the conductivity body under the WS volcano. (a)-(c) show the comparison of response curves at MT sites 2-8, 2-10, and 3-7, respectively. Red squares and blue triangles denote the resistivity and phase observations; Red and blue solid lines are theoretical curves from the originally inverted resistivity model; Red and blue dotted lines represent theoretical curves from modified resistivity model, which is formed by replacing the conductive body marked with the white rectangle in (d) for depths 5-15 km. (d) Locations for the three MT sites in (a)-(c) are shown as green triangles at the horizontal slice of resistivity model at 10 km. Other MT sites are shown as white circles.

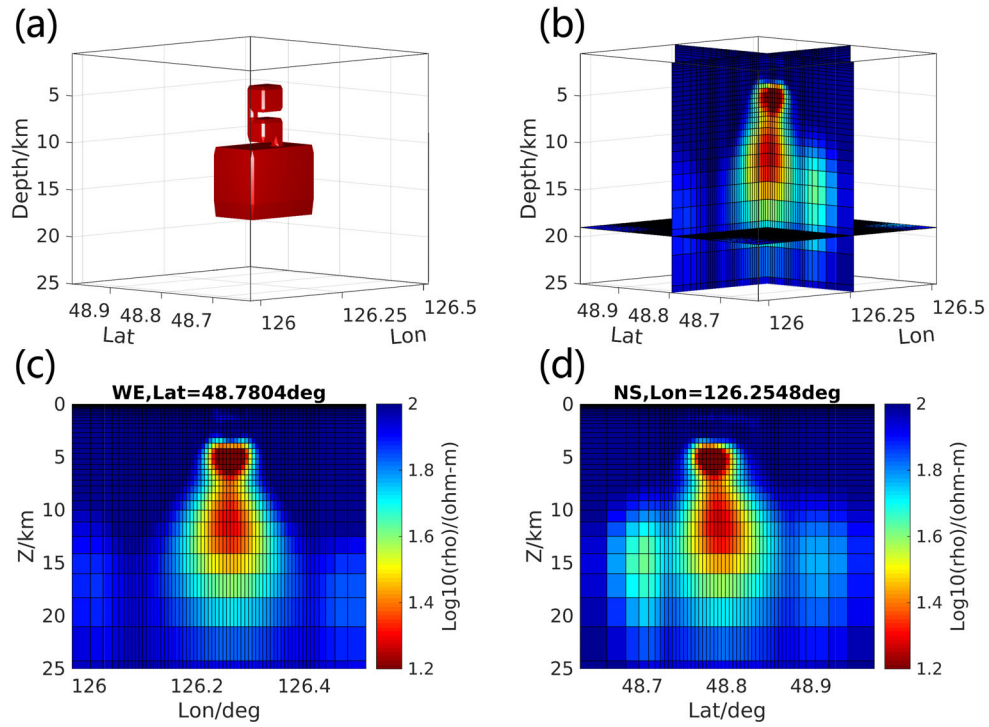


**Figure S6.** Synthetic test for a 3D model with low resistivity anomalies extended to 15 km depth. (a) Three-dimensional synthetic model with low resistivity anomalies of 10 ohm-m in a background of 100 ohm-m. The low resistivity anomalies consist of three parts in depth: 4.5-6.5 km, 7.5-9.5 km, and 11-16 km. The shallower two parts are smaller than the deepest part. (b) Inverted resistivity model with the same data distribution and inversion parameters as the WS field data. (c) and (d) are two resistivity sections across the 3D inverted model at latitude 48.7804 and longitude 126.2548, respectively.

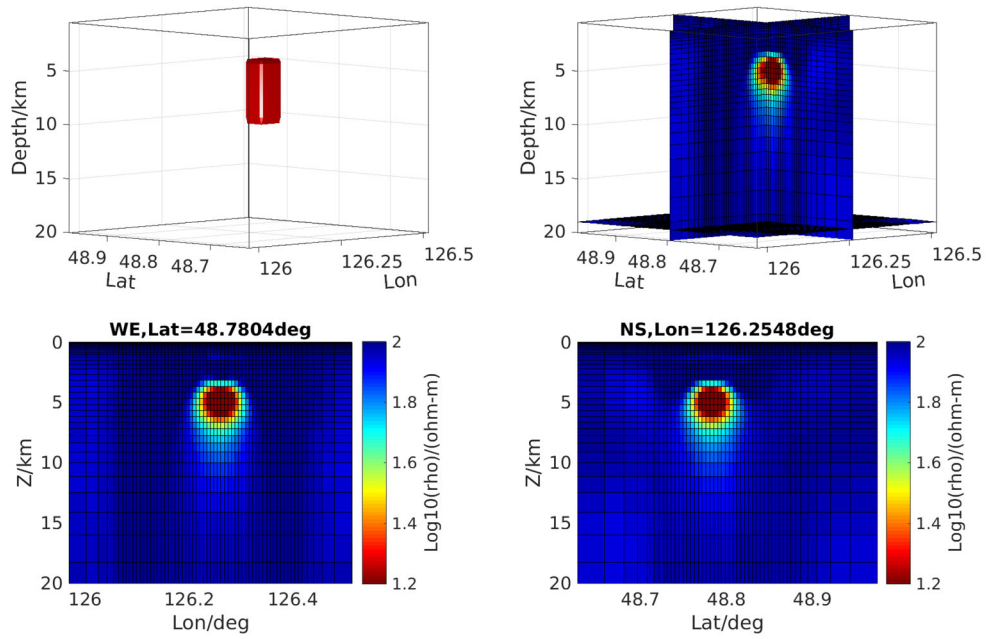


**Figure S7.** Synthetic test for a 3D model with low resistivity anomaly extended to 8 km depth. (a) Three-dimensional synthetic model with the low resistivity anomaly of 10 ohm-m in a background of 100 ohm-m. (b) Inverted resistivity model with the same MT data distribution and inversion parameters as the WS field data. (c) and (d) are two resistivity sections across the 3D model at latitude 48.7804 and longitude 126.2548, respectively.

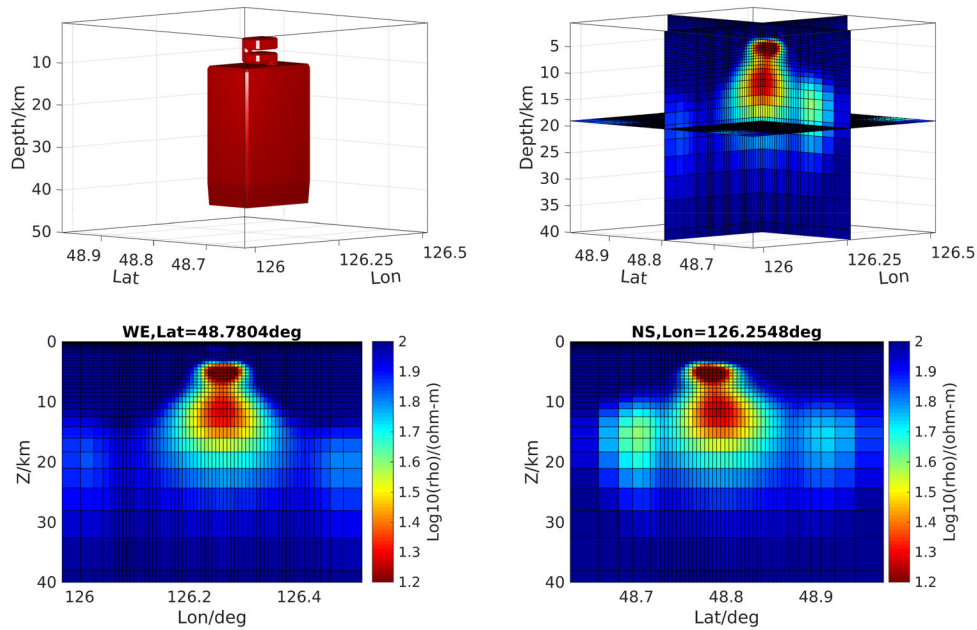


**Figure S8.** Synthetic test for a 3D model with low resistivity anomaly extended to 45km depth. (a) Three-dimensional synthetic model with the low resistivity anomaly of 10 ohm-m in a background of 100 ohm-m. The low resistivity anomalies consist of three parts in depth: 4.5-6.5 km, 7.5-9.5 km, and 11-45 km. The shallower two parts are smaller than the deepest part. (b) Inverted resistivity model with the same MT data distribution and inversion parameters as the WS field data. (c) and (d) are two resistivity sections across the resistivity model at latitude 48.7804 and longitude 126.2548, respectively.

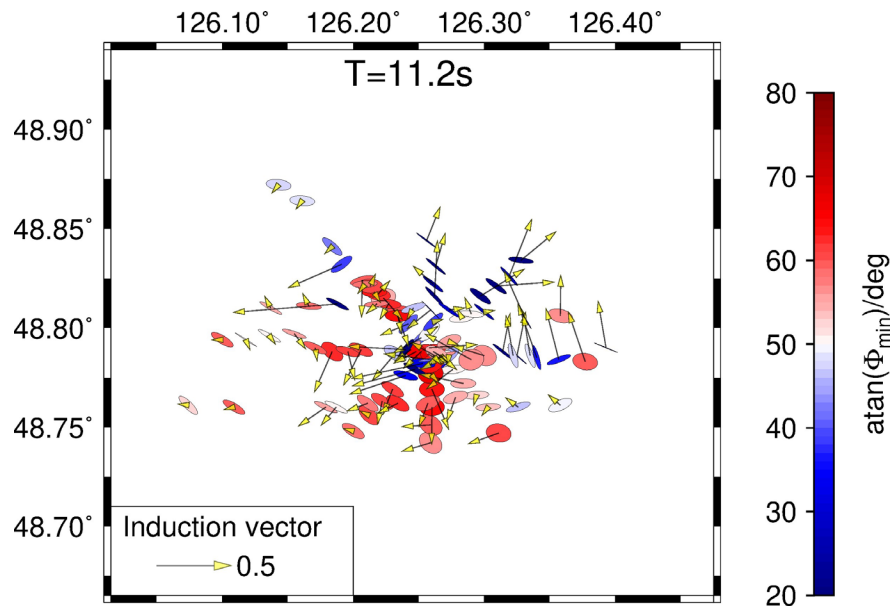


**Figure S9** Distribution of MT phases tensors at each site for the period of 11.2 s. The phase tensor ellipses are coloured according to the minimum phase value that denotes the variation of resistivity. Arrows represent real induction vectors, pointing away from low resistivity.

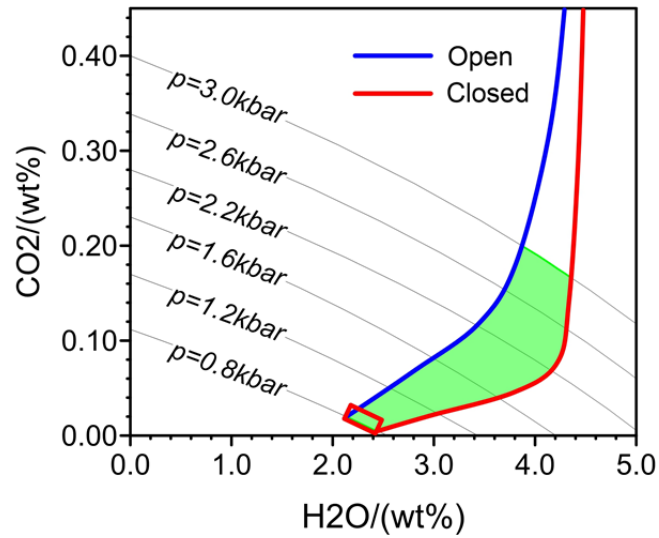


**Figure S10.** Modelled H<sub>2</sub>O-CO<sub>2</sub> degassing curves for the WVF magma. The red and blue curves represent degassing in closed and open systems, respectively. These curves are calculated using the model of Duan (2014) and the HSS5 melt composition based on the method of Di et al. (2019). The gray contours are H<sub>2</sub>O-CO<sub>2</sub> solubility isobars calculated following the method described in Di et al. (2019). Red rectangle indicates the water content corresponding with the depth of ~2.5 km beneath the Weishan volcano. The pressure is calculated by using the density derived from the Vs model beneath the Weishan volcano cone.

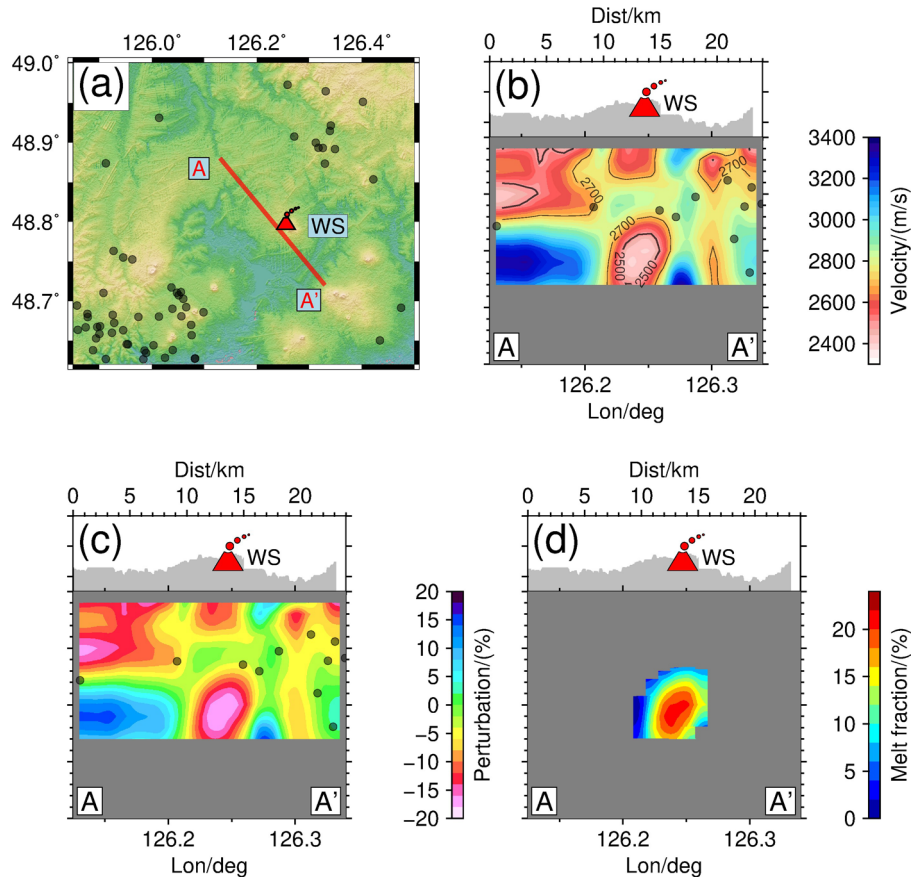


**Figure S11.** Melt fraction estimation based on the velocity anomalies along the section AA'. (a) Distribution of earthquakes (black dots) around the WS volcano. Location of AA' is denoted as a red line. (b) Cross section of the  $V_s$  model along AA' from ambient noise tomography of Li et al. (2016). (c) Velocity perturbations with respect to the background velocity of 3000 m/s. (d) Melt fraction estimation by using the relation between melt fraction and velocity anomaly of Flinders et al. (2018). Note only the magma-related velocity anomalies are used to estimate melt fractions.

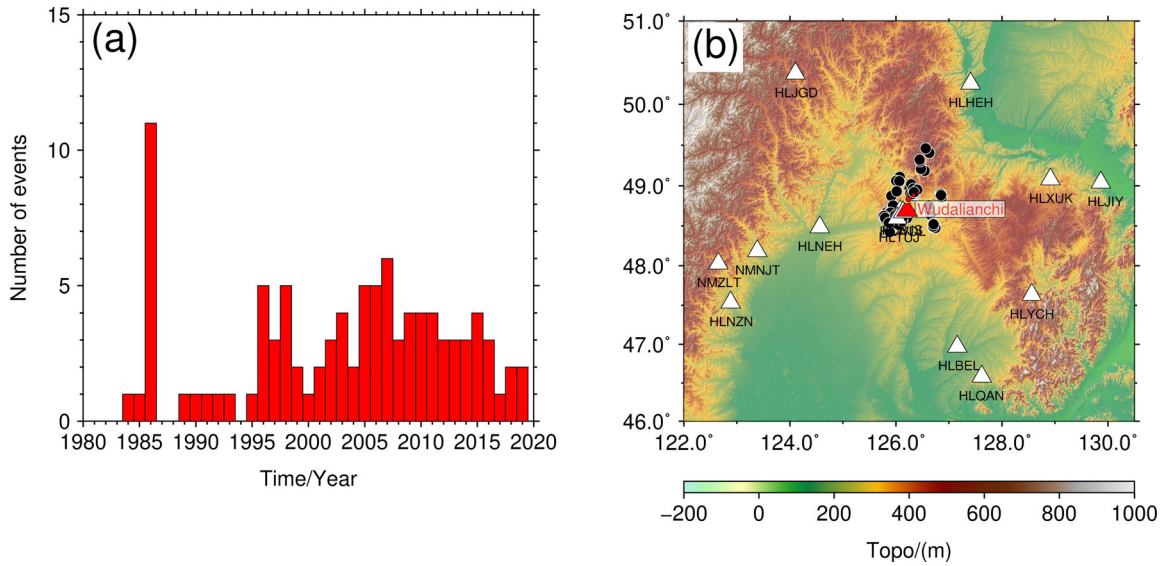


**Figure S12.** Earthquake activity around the WS volcano. (a) Earthquake frequency per year from 1980 to 2019 from the China Earthquake Administration (CEA) catalogue. (b) Distribution of permanent seismic stations (white triangles) and relocated earthquakes (black dots). Only 101 earthquakes having waveforms available for the period of 2008 to 2019 from the CEA data center are relocated.

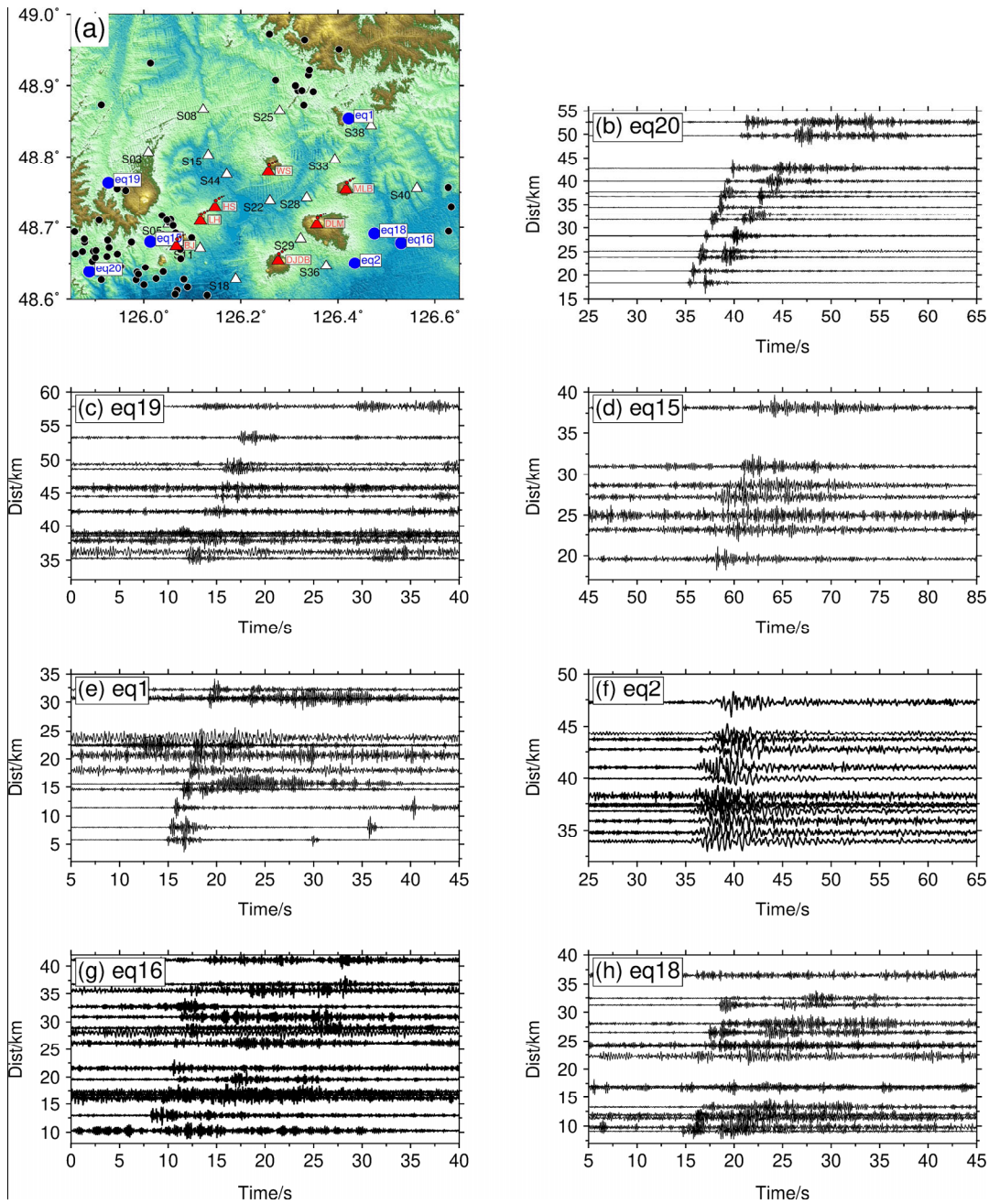


**Figure S13.** Distribution of selected seismic stations of temporary seismic array around the WS volcano of Li et al. (2016) and detected events, as well as their waveforms. (a) Distribution of temporary seismic stations (white triangles) and seismic events (dots). Blue dots represent the detected seven events and black dots indicate earthquakes relocated from the CEA catalogue from 2008 to 2019. (b) - (h) are Seismic waveforms for detected seismic events from the temporary seismic array. The event IDs are shown in (a) and Figure 1b.